Enhanced Performance of InAs-based Interband Cascade Lasers Emitting between 10-13 µm

Jeremy A. Massengale[1,2], Yixuan Shen[1], Rui Q. Yang[1], Samuel D. Hawkins[3], and John F. Klem[3]

[1] School of Electrical and Computer Engineering, University of Oklahoma, Norman, OK 73019, USA
[2] Homer L. Dodge Department of Physics and Astronomy, University of Oklahoma, Norman, OK 73019, USA
[3] Sandia National Laboratories, PO Box 5800, Albuquerque, NM 87185-1085, USA

E-mail: massengalej@ou.edu

Received xxxxxx
Accepted for publication xxxxxx
Published xxxxxx

Abstract

Interband cascade lasers (ICLs) based on the type-II quantum well (QW) active region have attracted much attention for a range of practical applications in the mid-infrared (MIR) due, in part, to their low power consumption. However, extending the operating wavelength of these ICLs into the long-wave infrared (LWIR) region presents several challenges including the reduced thermal conductivity of the optical cladding layers and the diminished wavefunction overlap in the type-II QW. One solution to alleviate the former concern is to use InAs-based ICLs. To solve the latter problem, $InAs_{0.5}P_{0.5}$ barriers are introduced in the active region, which lowers the electronic energy level and allows for the InAs well width to be reduced at longer emission wavelengths. Here the advancement of long wavelength ICLs, made from four new InAs-based ICL wafers grown by molecular beam epitaxy (MBE), is reported. These ICLs lased in the wavelength range from 10 to 13 µm and showed significantly improved performance compared with previous ICLs, including the first demonstration of broad-area devices operating in continuous wave (cw) mode beyond 12 µm. These ICLs exhibited substantially increased output powers with reduced threshold voltages (V_{th}) and current densities (J_{th}). They operated at temperatures up to 40 K higher than previous ICLs at similar wavelengths.

Keywords: interband cascade laser, ICL, semiconductor laser, III-V materials, quantum wells, heterostructures

1. Introduction

Interband cascade lasers (ICLs) have become a staple source for efficient emission in the mid-infrared (MIR) region, due in large part to their low power consumption. The operation of the type-II ICL relies on interband transitions in type-II quantum wells (QWs) as well as a cascade configuration, which enhances the total gain (per current density) [1-5]. Because of its design, the ICL is immune from phonon scattering unlike its counterpart, the quantum cascade laser (QCL), and can therefore reach lasing with very low threhold current densities (J_{th}). These features are ideal for many technological applications including gas/chemical sensing, imaging, and industrial process control, as well as within the 3-5 µm and 8-12 µm atmospheric transmission windows for free-space optical communication [6-9].

 © xxxx IOP Publishing Ltd

ICLs on GaSb substrates have been well developed for operating in the 3-6 μm wavelength (λ) range, with devices exhibiting efficient room temperature operation [5]. However, extending this type of ICL to longer wavelengths is challenging for two main reasons. First, the InAs/AlSb superlattice (SL) required for the optical cladding needs to be thicker in order to accommodate the longer optical wave decay length. This increases the complexity of the molecular beam epitaxy growth (MBE) due to the increased number of shutter movements and growth time. Additionally, the InAs/AlSb SL has a low thermal conductivity, which results in increased heating for the thicker cladding. Second, the InAs QWs in the active region need to be wider, which leads to a reduced electron-hole wavefunction overlap as the electrons and holes are localized mainly in spatially distinct layers. This can cause the optical gain generated from the type-II interband transition to be insufficient to overcome the increased loss at longer wavelengths, rendering lasing unreachable.

One method to rectify this situation is to switch from a GaSb substrate to an InAs substrate. For the InAs-based ICL[4], the thickness of the InAs/AlSb SL can be greatly reduced with a waveguide that features undoped InAs separate confinement layers (SCLs) and heavily doped n^+-InAs plasmon cladding layers [10-13]. It should be pointed out that this plasmon-enhanced waveguide may also be achieved on GaSb substrates by using heavily doped n^+-InAsSb latticed matched to GaSb and GaSb SCLs, but at the cost of more complicated carrier transport and MBE growth [4,14-15]. This approach in InAs-based ICLs allowed for pulsed lasing above room temperature near 7.1 μm [16] and extended the lasing operation to 11.1 μm, though with a relatively large threshold current density (J_{th}) at 80 K of 95 A/cm^2 [17]. More recently the advanced waveguide structure, originally developed for InAs ICLs emitting near 4.6 μm [18] and which places a relatively thin InAs/AlSb SL sandwiched between the InAs SCL and n^+-InAs plasmon cladding, was incorporated into InAs-based ICLs designed to emit near 11 μm and resulted in a four fold reduction in the J_{th} compared with previous ICLs at similar wavelengths [19].

To alleviate the reduced wavefunction overlap in the QW active region for devices operating at longer wavelengths, $InAs_{0.5}P_{0.5}$ barriers were introduced [19]. This phosphorus containing alloy has a lower valence band edge than that of the commonly used AlSb barrier and serves to lower the electronic state in the InAs QW, resulting in a reduced interband transition energy for photons at longer wavelengths [20]. Recently an InAs-based ICL which incorporated this feature was shown to exhibit pulsed lasing emission beyond 13 μm, which is the longest emission wavelength among all III-V interband lasers [19]. However, the extracted external quantum efficiency (EQE) of this device was quite low at 80 K (~ 41%), which was inferred to be due to high optical internal losses related to free carrier absorption and intersubband transitions in the valence band QWs.

In this work, we report the study of four 20-stage InAs-based ICLs with refinements to the waveguide and cascade region design based on the results in Ref. 19, with the goal of enhanced long wavelength operation in the 10-13 μm range.

2. Structure Design of InAs-based ICLs

For a comparative study, four ICL wafers (EB7541, EB7547, EB7523 and EB7539) were grown by MBE on InAs substrates, all of which incorporated the advanced waveguide, and two of which (EB7523 and EB7539) included the $InA_{0.5}P_{0.5}$ barriers in the QW active region. For EB7541 (EB7547), a regular W-QW structure [21-23] was used, consisting of a layer sequence of $AlAs_{0.89}Sb_{0.11}$/InAs/$Ga_{0.65}In_{0.35}Sb$/InAs/$AlAs_{0.89}Sb_{0.11}$, with thicknesses of 22/35(36.5)/28/31(31.5)/12 Å. For EB7523 (EB7539), the active region had a layer sequence of $AlAs_{0.89}Sb_{0.11}$/$InA_{0.5}P_{0.5}$/InAs/$Ga_{0.65}In_{0.35}Sb$/InAs/$InA_{0.5}P_{0.5}$, with thicknesses of 19/16/25(26)/28/20/16 Å in the growth direction. Here the InAs layer thicknesses in the latter wafers were reduced by about 30% in the first InAs QW and about 35% in the second InAs QW compared to the devices which did not include $InA_{0.5}P_{0.5}$ barriers. Based on a 2-band k·p model [24-25], the estimated wavefunction overlaps for EB7541 and EB7547 were 16.7% and 15.6%, respectively. The inclusion of the $InA_{0.5}P_{0.5}$ barriers in the QW active region in EB7523 and EB7539 increased the estimated overlap to 19% and 18.2%, respectively. The band edge diagrams of one cascade stage for each of the two representative device structures (EB7541 and EB7523) are shown in figures 1 and 2.

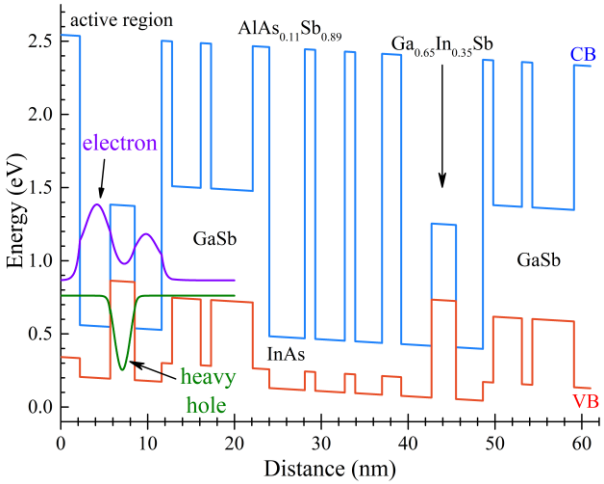

Figure 1. Band edge diagram for one cascade period of EB7541/EB7547, which do not include $InA_{0.5}P_{0.5}$ barriers in the QW active region.

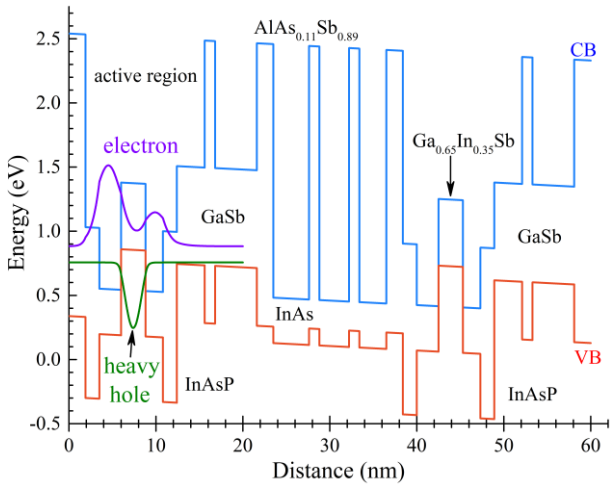

Figure 2. Band edge diagram for one cascade period of EB7523/EB7539, which include $InA_{0.5}P_{0.5}$ barriers in the QW active region.

In the previous work [19], there were some uncertainties in the expected operating wavelength for InAs-based ICLs that incorporated the advanced waveguide and those that utilized the modified QW active region, which chiefly manifested in high internal absorption losses, leading to relatively large J_{th}'s, low EQEs, low output powers, and limited temperature performance. Therefore, several adjustments to the waveguide were made to reduce the internal loss and to better confine the optical wave within the QW active region. Since the expected emission for these ICLs was to be beyond 11 µm at higher operating temperatures, the waveguide layer thicknesses were slightly increased. Compared to the previous design [19], the thicknesses of the individual components were increased by about 18%, 5%, and 7% for the InAs SCL, InAs/AlSb SL intermediate cladding, and the n^+-InAs plasmon cladding layers, respectively. To further reduce losses due to free carrier absorption in the n^+-InAs plasmon cladding, the doping concentration there was reduced by about 13%. Also, the doping in the injection region was reduced by about 31%. The calculated optical modal profile and refractive index based on a slab waveguide model for a representative device (EB7541) are shown in figure 3. In each of the SL intermediate cladding layers, to reduce the free-carrier absorption loss, there are two segments with different doping levels. The segment that is closer to the cascade region has lower doping resulting in a slightly higher real part of its refractive index. Depicted in figure 3 are the waveguide loss (α_{wg}), estimated threshold gain (G_{th}), the effective refractive index of the entire waveguide (n_{eff}), and the optical confinement factor (Γ). In the simulation, the internal loss (waveguide loss) is calculated based only on free carrier absorption, which gives a lower bound estimate to the overall internal loss within the device. The emission wavelength λ of each device was measured at 80 K in pulsed mode operation, which prevented potential redshifts that could be caused by local heating, and used in the waveguide simulations. The various optical parameters based on the waveguide simulations of the other devices reported here are listed in table 1.

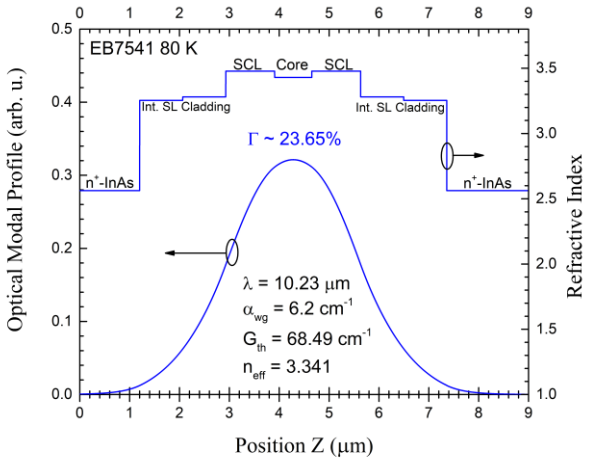

Figure 3. Calculated optical modal profile and refractive index of the waveguide for EB7541 at 80 K with an emission wavelength λ measured from the pulsed spectra of 10.2 µm.

Device Name	InAsP Barriers-InAs QW thickness (Å)	80 K λ (µm)	Γ (%)	α_{wg} (cm^{-1})	G_{th} (cm^{-1})	n_{eff}
EB7541	No-35/31	10.2	23.65	6.2	68.49	3.341
EB7547	No-36.5/31.5	10.9	23.33	7.3	74.15	3.324
EB7523	Yes-25/20	11.8	22.61	8.7	82.69	3.300
EB7539	Yes-26/20	12.1	22.39	9.3	86.19	3.292

Table 1. Calculated optical parameters of the four 20-stage InAs-based ICLs studied, with the 80 K emission wavelength λ measured from the pulsed spectra.

3. Growth Characterization of InAs-based ICLs

The ICL wafers were grown by molecular beam epitaxy using solid sources except for P, which was supplied by a cracking phosphine injector. All layers were grown at 440 °C. Growth rates were approximately 1.0 µm/hr for InAs and InAsP and 0.49 µm/hr for AlAsSb, GaInSb, and GaSb. The cladding layers were nominally InAs/AlSb superlattices, but since the As source valve was left open during the cladding AlSb layer growth and the As source shutter does not fully block the As flux, layers nominally grown as AlSb contained substantial As, which was accounted for in separate lattice matching calibration growths. The As source valve was closed during critical portions of the active region growth.

The material quality was analyzed using x-ray diffraction (XRD), and the surface morphology was characterized by differential interference contrast (DIC) microscopy. The

XRD spectra were measured using a Panalytical X'Pert3 MRD. Symmetric scans along the (004) axis were obtained and show reasonable agreement with the simulated spectra, as detailed in figure 4. From the XRD spectra, the InAs/AlSb SLs of all four ICL wafers show a slight compressive strain in the growth direction (biaxial tensile strain), with a substrate/SL zero-order peak separation ranging between 14-50 arcsec, corresponding to a lattice mismatch of 0.12-0.17%. The InAs/AlSb SL thickness across each of the four ICL wafers range from 0.12% thinner to 0.5% thicker, compared to the intended design. The cascade region was consistently thinner among all four wafers, ranging from 0.5%-1.3%, compared with the design.

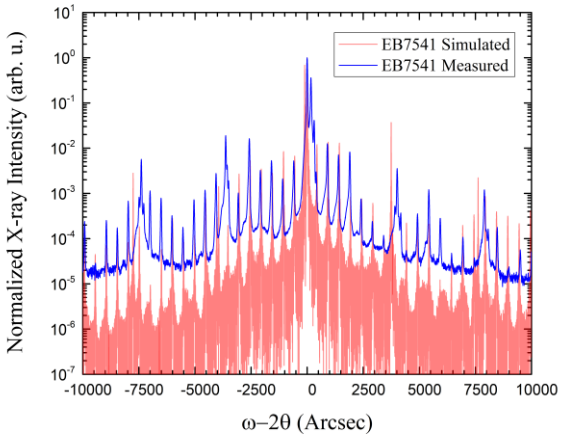

Figure 4. Measured XRD spectrum (blue, top) compared to the simulated spectrum (red, bottom) for ICL wafer EB7541.

From surface images on the four wafers, typical oval hillock defects were observed - common to III-V ICL growth, but with little background surface roughness. The surface defect density was measured at four different locations on each of the wafers grown. The average defect density across all wafers ranged from 1.2-9.2×10^4 cm^{-2}, which are within acceptable limits for reasonable device performance.

The grown wafers were fabricated into 100-µm-wide (e.g. EB7523BA3-2F, EB7539BA2-2D, EB7541BA3-3H, and EB7547BA3-2A) and 150-µm-wide (e.g., EB7541BA3-1G, EB7547BA3-3C, EB7539BA2-2A) broad area (BA) mesas using standard UV contact photolithography and wet chemical etching. The wafers were left unthinned and cleaved into approximately 1.5-mm-long laser bars without facet coating, which were mounted epi-side up on copper heat sinks for testing.

4. ICL Device Testing

The fabricated devices were tested using a Nicolet Fourier transform infrared spectrometer (FTIR), with cw power measurements carried out with a PM3 Coherent PowerMax thermopile power meter, in which the beam divergence loss was not included. Hence, the reported output power and EQE of the devices are conservative. Multiple devices from each of the four ICL wafers operated in both cw and pulsed modes, as shown in figure 5. All characteristics presented in this work are from representative devices among the many tested. Of the four ICL wafers grown, EB7541 and EB7547 are most directly related for comparison purposes as they include only the advanced waveguide. EB7523 and EB7539 include both the advanced waveguide as well as the modified QW active region. ICLs made from them have significantly longer emission wavelengths than those of EB7541 and EB7547, and consequently their threshold current densities are larger as reflected in Fig. 5. Detailed characteristics of their device performance will be presented in the following two subsections and further discussion will be given in section 4.

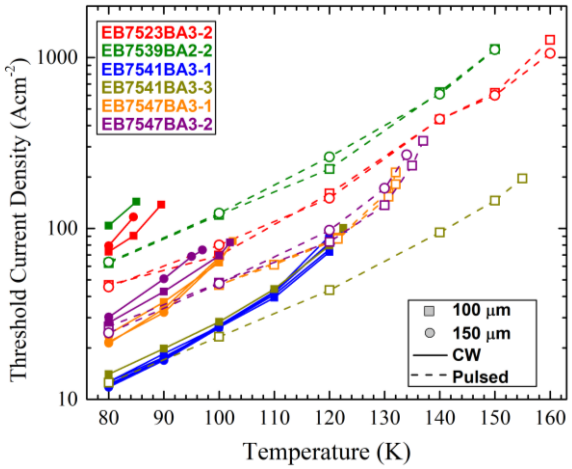

Figure 5. Threshold current density (J_{th}) as a function of temperature for several devices made from the four InAs ICL wafers.

4.1 EB7541 and EB7547

Wafers EB7541 and EB7547 both included the advanced waveguide but did not include $InA_{0.5}P_{0.5}$ barriers in the QW active region. In cw mode, two devices from EB7541 had threshold current densities as low as 12 A/cm^2 at 80 K, representing about a 50% reduction compared to previous ICLs operating at similar wavelengths [19]. These ICLs lased at 10.2 µm at 80 K and then red-shifted to longer wavelengths at high temperatures. The characteristics of a representative device, EB7541BA3-3H, are shown in Fig. 6. This device operated in cw mode up to 123 K, about 17 K higher than a previous ICL, with an emission wavelength of 10.9 µm and a J_{th} of about 101 A/cm^2. This device exhibited a significant increase in the measured cw output power at 80 K, just over 56 mW/facet, about four times as much as a previous ICL [19], as shown in figure 6(a). The cw output power of 43 mW/facet at 200 mA is more than twice that (15 mW/facet) from an early ICL at the shorter lasing wavelength of 9.1 µm at 80 K and at the same curent [26].

Compared to previous devices (V_{th} ~ 9.2 V at 80 K) reported in Ref. 19, the cw threshold voltage was reduced by a factor of 2 (V_{th} ~ 4.6 V at 80 K), resulting in a voltage efficiency of about 53%. However, this is still substantially less than the voltage efficiency of ~80% observed in early ICLs, which had smooth carrier transport [4, 17, 26], suggesting room for further improvement. The extracted EQE under cw operation reached ~ 592% at 80 K, indicating the cascaded emission of photons in the ICL, and dropped to ~ 78% at 123 K as shown in figure 6(a). Under pulsed operation, this device lased up to 155 K near 11.2 μm (Fig. 7) with a J_{th} of 196 A/cm^2, where the voltage efficiency dropped to 49% with a V_{th} of 4.52 V. The extracted EQE under pulsed operation reached ~ 640% at 80 K, subsequently dropping to 137% at 150 K, as shown in figure 7. The difference in the EQE at 80 K between cw and pulsed modes is attributed to heating in the active region of the device. The heating effect increased with the higher threshold current when the heat-sink temperature was raised, which was reflected by the greater decrease of the EQE in cw operation compared to that in pulsed operation, as shown in Fig. 6 and Fig. 7.

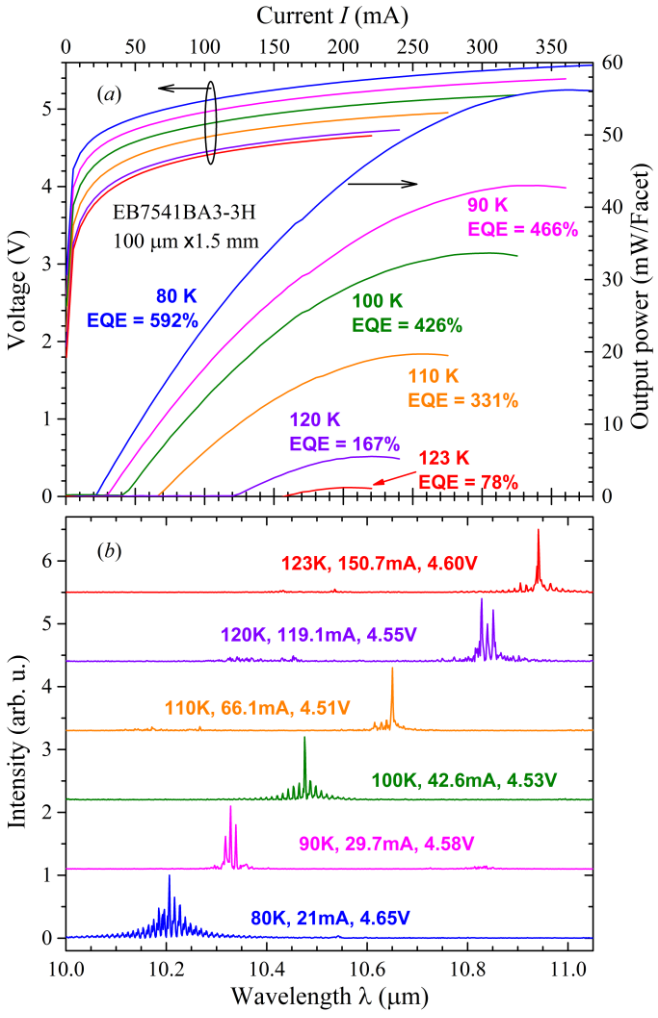

Figure 6. CW results for the current-voltage-power (IVL) characteristics (a) for EB7541BA3-3H along with the cw emission spectrum (b) between 80 K and 123 K.

Compared to ICLs from EB7541, devices from wafer EB7547 lased at longer wavelengths as expected due to the slightly wider InAs QWs, and they had higher J_{th} and somewhat degraded temperature performance as shown in Fig. 5. In cw mode, a representative device, EB7547BA3-2A, lased at 10.9 μm at 80 K, with a J_{th} of 26.7 A/cm^2 and a V_{th} of 4.9 V. This ICL delivered output power of 32 mW/facet as shown in Fig. 8, higher than any interband laser has achieved at such a long wavelength. EB7547BA3-2A lased up to 102 K in cw mode at 11.3 μm with an EQE of 189% (Fig. 8), still exceeding the conventional limit of unity and indicating the potential for higher temperature operation. This device lased up to 137 K in pulsed mode at a J_{th} of 325 A/cm^2 and with a lasing wavelength of 11.5 μm as shown in Fig. 9, which is the longest among ICLs with the regular W-QWs. The extracted EQE in pulsed mode at 80 K for this device was 552%, which is comparable to that of EB7541BA3-3H.

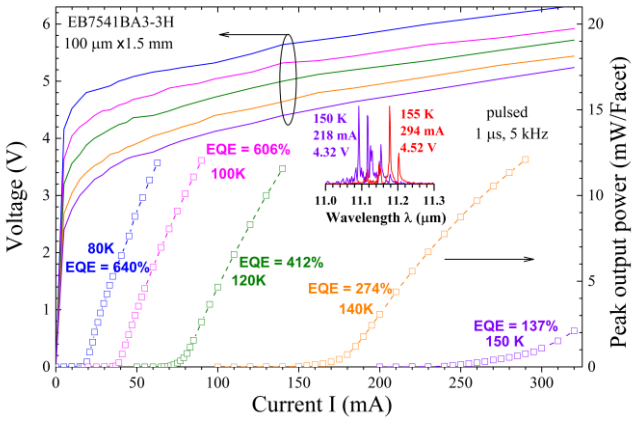

Figure 7. Pulsed current-voltage-power (IVL) characteristics for EB7541BA3-3H with the lasing spectrum (inset) at 150 and 155 K.

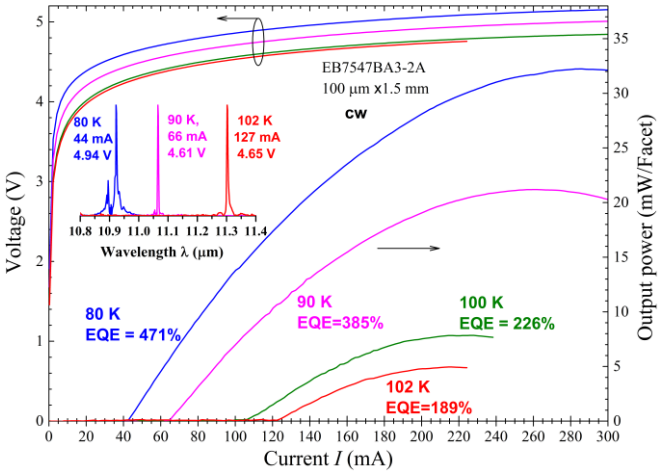

Figure 8. Current-voltage-power (IVL) characteristics for EB7547BA3-2A in cw mode. The inset shows the cw lasing spectrum between 80 K and 102 K.

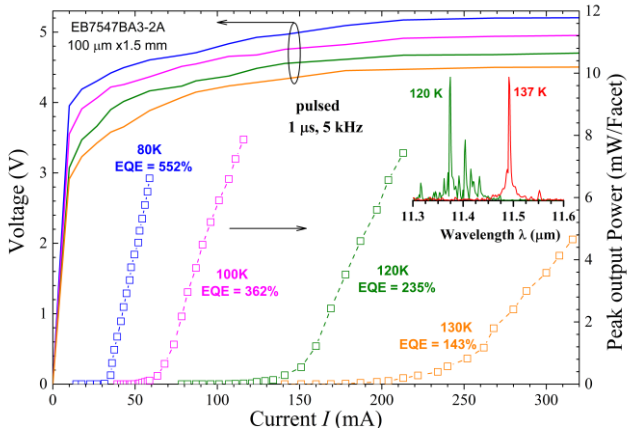

Figure 9. Pulsed current-voltage-power (IVL) characteristics for EB7547BA3-2A with the lasing spectrum (inset) at 120 and 137 K.

Considering both wafers had the same waveguide, doping concentrations, and nearly identical active region designs, the small difference in the InAs QW width only resulted in an approximately 6.9% shift of lasing wavelength at 80 K. Hence, similar band structure, differential gain and transparency current density would be expected for both. Consequently, they should have comparable threshold current density. This is also due to the fact that the free-carrier absorption loss difference between them is less than 20% based on the simulation shown in Table 1, which is supported by the comparable EQEs observed for them at 80 K, as shown in Figs. 7 and 9. However, the J_{th} at 80 K in devices from EB7547 are about twice that compared to devices from EB7541, very different from the above perspectives and the observed insensitivity of the J_{th} at low temperatures (e.g., 80K) on the lasing wavelength for early ICLs [2,13]. This suggests that extra factors beyond free carrier loss played a role in determining the J_{th} for devices from EB7547, which will be a subject of our future research. In addition to the higher J_{th}, another issue in EB7547BA3-2A is that the EQE decreased relatively fast with the increase of temperature as shown in Fig. 9. Nevertheless, despite the higher J_{th}, its maximum operating temperature was only 18 K lower in pulsed mode than that of EB7541BA3-3H, since it could lase with a higher J_{th} than EB7541BA3-3H (325 A/cm^2 vs 196 A/cm^2). Compared to the previous ICL in Ref. 19, though improvements have been made, the maximum allowable J_{th} in devices from both wafers is still relatively small in contrast to other ICLs. This limited their maximum operating temperature in cw and pulsed modes

4.2 EB7523 and EB7539

Wafers EB7523 and EB7539 both included the advanced waveguide as well as the $InA_{0.5}P_{0.5}$ barriers in the QW active region. Multiple devices from both wafers lased in both cw and pulsed modes. A representative device EB7523BA3-2F lased in cw mode up to 90 K, with an emission wavelength of 12.2 µm and a J_{th} ~ 138 A/cm^2 as shown in Fig. 10. This is a significant milestone as it is the first demonstration of a BA ICL operating in cw mode, beyond 12 µm. Furthermore, the maximum obtainable output power at 80 K was 12 mW/facet (Fig. 10), which is comparable to and even higher than that of the previous ICLs (without $InA_{0.5}P_{0.5}$ barriers) at shorter wavelengths (10.8 and 10.2 µm) [17, 19]. At 80 K the V_{th} was about 6.8 V, corresponding to a voltage efficiency of about 31%. This low voltage efficiency indicates that there are likely issues in the carrier transport for ICLs containing $InA_{0.5}P_{0.5}$ barriers. The extracted EQE at 80 K in cw mode reached 214%, as shown in figure 10 and validated the cascade process in ICLs with InAsP barriers for the first time.

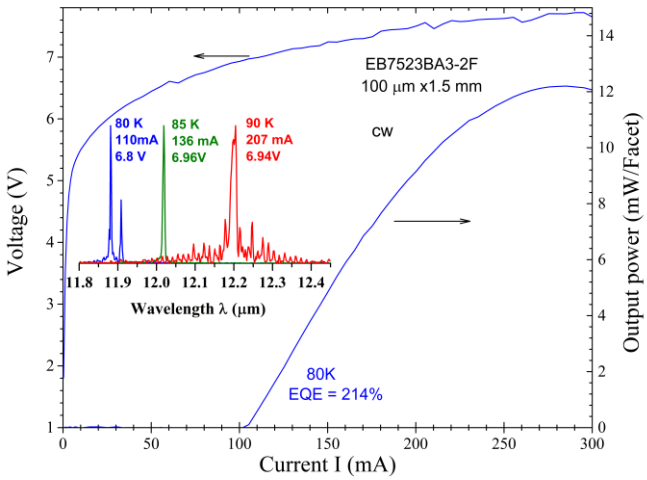

Figure 10. Current-voltage-power (IVL) characteristics for EB7523BA3-2F in cw mode. The inset shows the cw emission spectrum between 80 K and 90 K.

In pulsed mode, this device lased at 80 K at 11.8 µm, with a J_{th} ~ 44 A/cm^2, which was reduced by a factor of nearly 4 compared to the previous ICL [19], while its EQE reached 451% at 80 K (Fig. 11), which is much higher than that (41%) in the initial ICL containing $InA_{0.5}P_{0.5}$ barriers [19]. Additionally, this device operated in pulsed mode up to 160 K at 12.97 µm with a J_{th} ~ 1267 A/cm^2, an increase of 40 K compared to the previous ICL [19]. Although this ICL lased at longer wavelengths near 13 µm, the operating temperature (160 K) of this device was even higher than the maximum pulsed operating temperature of ICLs at shorter wavelengths from wafers EB7541 and EB7547. These significant improvements suggest further potential of ICLs containing $InA_{0.5}P_{0.5}$ barriers.

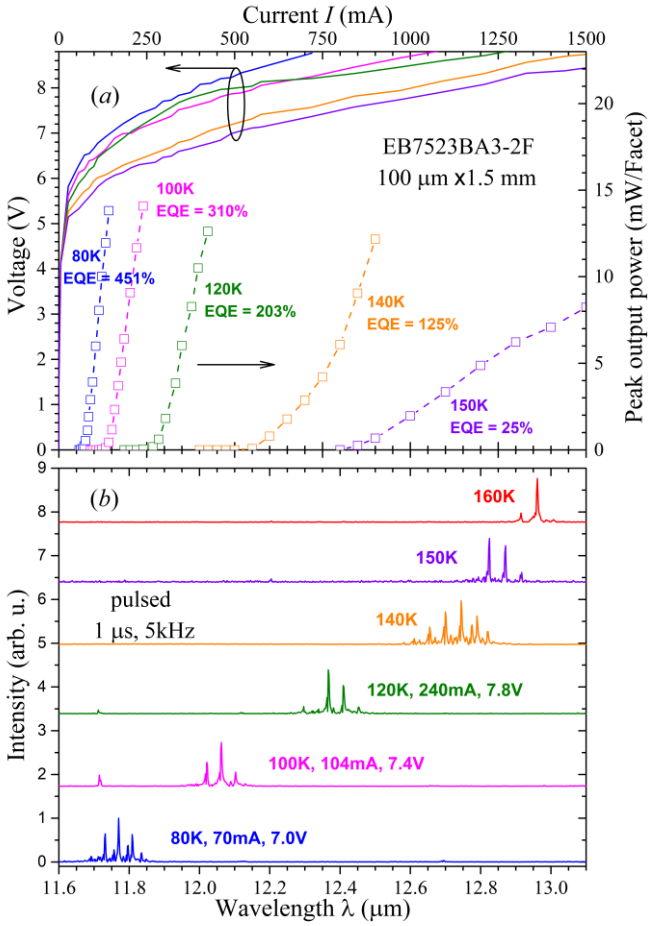

Figure 11. Pulsed results for the current-voltage-power (IVL) characteristics (a) for EB7523BA3-2F along with the pulsed emission spectrum (b) between 80 K and 160 K.

A representative 100-µm-wide device from wafer EB7539 also operated in cw mode up to 85 K with a J_{th} ~ 143 A/cm^2 and at a lasing wavelength of 12.4 µm (Fig. 12), longer than devices from EB7523 and consistent with the design. It delivered an output power of 6.4 mW/facet at 80 K with a V_{th} of about 5.7 V, which corresponds to a voltage efficiency of ~ 35%, similar to devices from EB7523.

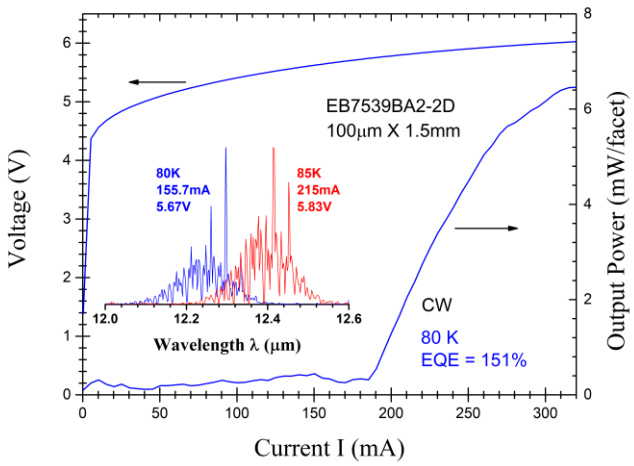

Figure 12. Current-voltage-power (IVL) characteristics for EB7539BA2-2D in cw mode. The inset shows the cw emission spectrum between 80 K and 85 K.

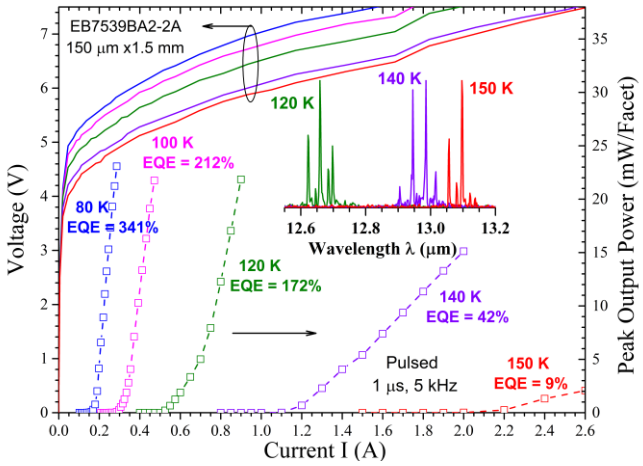

Figure 13. Current-voltage-power (IVL) characteristics for EB7539BA2-2A in pulsed mode. The inset shows the pulsed emission spectrum between 120 K and 150 K.

In pulsed operation, a 150-µm-wide device (EB7539BA2-2A) lased at 80 K with a J_{th} ~ 64 A/cm^2, which is reduced about three times compared to the previous ICL with InAsP layers [19], and 45% higher than that of EB7523BA3-2F. Furthermore, this device lased in pulsed mode up to 150 K at 13.1 µm with a J_{th} ~ 1111 A/cm^2. The extracted EQE in pulsed mode was ~ 341% at 80 K before dropping to ~ 9% at 150 K as shown in figure 13. Both EB7523 and EB7539 were able to hold significanly more current density at their maximum operating temperature compared with EB7541 and EB7547. Also, their differences in EQE and threshold current density are seemingly more mutually consistent in quantitative scale with their difference in the estimated free-carrier absorption loss shown in Table 1, in contrast to the differences between EB7541 and EB7547.

5. Further Discussion

From the data presented, several additional quantities may be inferred. The effective refractive index (n_{eff}) of each device, based on the waveguide simulation, can be used to estimate the facet reflectance ($R_{1,2}$) and the subsequent mirror loss (α_m). Using EB7541BA3-3H as an example, the estimated $R_{1,2}$ and α_m values are 0.291 and 8.236 cm^{-1}, respectively. Since the waveguide simulation estimates a lower bound (LB) for the internal loss (α_i), an upper bound (UB) can be estimated as well. Considering pulsed mode operation at 80 K and assuming a perfect internal quantum efficiency (IQE), the upper bound values of the α_i can be obtained based on the extracted EQE for each device and the calculated α_m. In the case of EB7541BA3-3H, a perfect IQE is equal to $N_c \times 100\% = 2000\%$, where N_c is the number of cascade stages in the device. Based on this assumption, an upper bound value of the α_i would be 17.5 cm^{-1}. Furthermore, a lower bound of the IQE can be determined based on the calculated α_m, the measured EQE, and the lower bound α_i from the waveguide simulation. For EB7541BA3-3H, this results in a lower bound IQE of 1122%, considering a waveguide loss due only to free carrier absorption of 6.2 cm^{-1}. By utilizing the estimated optical confinement factor (Γ) attained from the waveguide simulation, as well as the α_m, and the upper and lower bounds for the α_i, an estimation of the upper and lower bounds for the threshold gain (g_{th}) can be ascertained. For EB7541BA3-3H, the resulting lower and upper bounds for the g_{th} are 61.0 cm^{-1} and 108.8 cm^{-1}, respectively. Table 2 lists these various estimated properties from the above discussion for the other devices presented in this work.

Device	I_{th} (mA)	$R_{1,2}$	α_m (cm^{-1})	UB α_i (cm^{-1})	LB IQE	UB g_{th} (cm^{-1})	LB g_{th} (cm^{-1})
EB7541	19	0.291	8.236	17.5	1122%	108.8	61.0
EB7547	43	0.289	8.281	21.7	1039%	128.6	66.8
EB7523	66	0.286	8.345	28.7	921%	163.7	75.4
EB7539	94	0.285	8.367	49.3	612%	257.7	78.9

Table 2. Several estimated device parameters based on measured results in pulsed mode at 80 K and the waveguide simulation.

Based on the experimental results presented here, it can be observed that the overall performance of the ICLs follows the order: EB7541, EB7547, EB7523, and lastly EB7539. This trend is qualitatively represented in the various quantities calculated in table 2. There it can be seen that the lower bound for the IQE across all 4 wafers is generally much lower than the ideal value (100% per stage). If the LB IQE are valid, there could be significant current leakage and non-radiative recombination lossess due to SRH and Auger processes. However, this is unlikely to be true for broad-area ICL devices at 80 K, where the required threshold carrier concentration is relatively low. Also, the defect density for the wafers is not high ($<10^5/cm^2$). Hence, actual internal losses present in these devices could be substantially higher than the estimated values based only on the free-carrier absorption loss. The extra aborption loss might be caused by intersubband transitions in valence band QWs [27-28], which was recently studied and confirmed in ICLs in the 4-7 μm wavelength region [29-30]. How intersubband transitions in the valence band could affect the device performance of LW InAs-based ICLs would be an interesting topic for future research.

A future iteration on this subject will consider further adjustments to the waveguide and QW layer thicknesses and doping concentrations. These adjustments should benefit the carrier transport and allow for the devices to carry larger currents and operate at higher temperatures. Furthermore, the same waveguide was used for all four ICL structures presented here. However, each ICL structure emits at a different wavelength, and so a unique waveguide tailored for the desired lasing wavelength at higher operating temperatures will further help to optimize the device performance.

6. Concluding Remarks

Four new InAs-based ICL wafers were grown, which included an advanced waveguide consisting of InAs SCLs, InAs/AlSb intermediate SL cladding, and n^+-InAs plasmon cladding layers. Two of the ICL wafers also included $InA_{0.5}P_{0.5}$ barriers in the QW active region to achieve longer wavelength operation. Modifications to the waveguide based on the previous work, which included layer thickness changes and doping concentration adjustments, resulted in enhanced device performance in the 10-13 μm wavelength region. Furthermore, the ICLs that included the active layer design change exhibited cw operation beyond 12 μm, which is the first demonstration of BA ICLs operating in cw mode at such long wavelengths. Several ICLs with this P-containing barrier have been explored with varying InAs and $InA_{0.5}P_{0.5}$ layer thicknesses, which have helped to pave the way for better understanding of the expected lasing wavelength for this new kind of ICL. For practical applications, these long wavelength ICLs need to be capable of operating near room temperature, or at least at temperatures accessible by thermoelectric cooling. Possible issues were identified, which suggest further room for refinement. Nonetheless, the improvements presented here are encouraging and we believe that with additional adjustments such ICLs should be able to achieve better performance in the 10-13 μm range at elevated temperatures.

Acknowledgements

The work at the University of Oklahoma was partially supported by NSF (No. ECCS-1931193). This work was performed, in part, at the Center for Integrated Nanotechnologies, an Office of Science User Facility operated for the U.S. Department of Energy (DOE) Office of Science. This article has been authored by an employee of

National Technology & Engineering Solutions of Sandia, LLC under Contract No. DE-NA0003525 with the U.S. Department of Energy (DOE). The employee owns all right, title and interest in and to the article and is solely responsible for its contents. The United States Government retains and the publisher, by accepting the article for publication, acknowledges that the United States Government retains a non-exclusive, paid-up, irrevocable, world-wide license to publish or reproduce the published form of this article or allow others to do so, for United States Government purposes. The DOE will provide public access to these results of federally sponsored research in accordance with the DOE Public Access Plan https://www.energy.gov/downloads/doe-public-access-plan. We thank Zhisheng Shi for lending a MCT detector used for the pulsed power testing.

References

[1] R. Q. Yang, "Infrared laser based on intersubband transitions in quantum wells," Superlattices Microstruct. 17, 77 (1995).

[2] R. Q. Yang, "Interband cascade (IC) lasers," in Semiconductor Lasers Fundamentals and Applications, edited by A. Baranov and E. Tournie (Woodhead Publishing, Cambridge, 2013), Chap. 12, pp. 487–513.

[3] J. Koeth, R. Weih, J. Scheuermann, M. Fischer, A. Schade, M. Kamp, and S. Höfling, "Mid infrared DFB interband cascade lasers," Proc. SPIE 10403, 1040308 (2017).

[4] R. Q. Yang, L. Li, W. Huang, S. M. Shazzad Rassel, J. A. Gupta, A. Bezinger, X. Wu, G. Razavipour, and G. C. Aers, "InAs-based interband cascade lasers," IEEE J. Sel. Top. Quantum Electron. 25, 1200108 (2019).

[5] J. R. Meyer, W. W. Bewley, C. L. Canedy, C. S. Kim, M. Kim, C. D. Merritt, and I. Vurgaftman, "The interband cascade laser," Photonics 7, 75 (2020).

[6] I. Vurgaftman, P. Geiser, W. W. Bewley, C. D. Merritt, C. L. Canedy, M. V. Warren, M. Kim, C. S. Kim, and J. R. Meyer, "Sensitive chemical detection with distributed feedback interband Cascade lasers," in Encyclopedia of Analytical Chemistry, edited by R. A. Meyers (Wiley, Chichester, 2016).

[7] J. Scheuermann, P. Kluczynski, K. Siembab, M. Straszewski, J. Kaczmarek, *et al*, "Interband Cascade Laser Arrays for Simultaneous and Selective Analysis of C1–C5 Hydrocarbons in Petrochemical Industry", Applied Spectroscopy **75** (3), 336-342 (2021).

[8] C. S. Goldenstein, R. M. Spearrin, J. B. Jeffries, and R. K. Hanson, "Infrared laser-absorption sensing for combustion gases," Prog. Energy Combust. Sci. 60, 132–176 (2017).

[9] A. Soibel, M. W. Wright, W. H. Farr, S. A. Keo, C. J. Hill, R. Q. Yang, and H. C. Liu, IEEE Photonics Technol. Lett. 22, 121 (2010).

[10] Z. Tian, R. Q. Yang, T. D. Mishima, M. B. Santos, R. T. Hinkey, M. E. Curtis, and M. B. Johnson, "InAs-based interband cascade lasers near 6 μm," Electron. Lett. 45, 48 (2009).

[11] Z. Tian, R. Q. Yang, T. D. Mishima, M. B. Santos, and M. B. Johnson, "Plasmon-waveguide interband cascade lasers near 7.5 μm," IEEE Photonics Technol. Lett. 21, 1588 (2009).

[12] R. T. Hinkey, Z. Tian, R. Q. Yang, T. D. Mishima, and M. B. Santos, "Reflectance spectrum of plasmon waveguide interband cascade lasers and observation of the Berreman effect," J. Appl. Phys. 110, 043113 (2011).

[13] R. Q. Yang, L. Li, L. Zhao, Y. Jiang, Z. Tian, H. Ye, R. T. Hinkey, C. Niu, T. D. Mishima, M. B. Santos, J. C. Keay, M. B. Johnson, and K. Mansour, "Recent progress in development of InAs-based interband cascade lasers," Proc. SPIE 8640, 86400Q (2013).

[14] C. L. Canedy, M. V. Warren, C. D. Merritt, W. W. Bewley, C. S. Kim, M. Kim, I. Vurgaftman, and J. R. Meyer, "Interband cascade lasers with longer wavelengths," Proc. SPIE 10111, 101110G (2017).

[15] Y. Lin, J. A. Massengale, W. Huang, R. Q. Yang, T. D. Mishima, and M. B. Santos, "Examination of the durability of interband cascade lasers against structural variations," J. Infrared Millimeter Waves 39, 137 (2020).

[16] M. Dallner, F. Hau, S. Hofling, and M. Kamp, "InAs-based interband cascade lasers emitting around 7 μm with threshold current densities below 1 kA/cm^2 at room temperature," Appl. Phys. Lett. 106, 041108 (2015).

[17] L. Li, H. Ye, Y. Jiang, R. Q. Yang, J. C. Keay, T. D. Mishima, M. B. Santos, and M. B. Johnson, "MBE-grown long-wavelength interband cascade lasers on InAs substrates," J. Cryst. Growth 425, 369 (2015).

[18] L. Li, Y. Jiang, H. Ye, R. Q. Yang, T. D. Mishima, M. B. Santos, and M. B. Johnson, "Low-threshold InAs-based interband cascade lasers operating at high temperatures," Appl. Phys. Lett. 106, 251102 (2015).

[19] J. A. Massengale, Y. Shen, R. Q. Yang, S. D. Hawkins, and J. F. Klem, "Long wavelength interband cascade lasers," Appl. Phys. Lett. 120, 091105 (2022).

[20] R. Q. Yang, "Electronic states and interband tunneling conditions in type-II quantum well heterostructures," J. Appl. Phys. 127, 025705 (2020).

[21] L. Esaki, L. L. Chang, and E. E. Mendez, "Polytype superlattices and multi-heterojunctions", Jpn. J. Appl. Phys., **20**, L529 (1981).

[22] J.R. Meyer, C.A. Hoffman, F.J. Bartoli, L.R. Ram-Mohan, "Type-II quantum-well lasers for the mid-wavelength infrared", Appl. Phys. Lett., **67**, 757 (1995).

[23] C. L. Felix, W. W. Bewley, E. H. Aifer, I. Vurgaftman, J. R. Meyer, C.-H. Lin, D. Zhang, S. J. Murry, R. Q. Yang, and S. S. Pei, "Low threshold 3 μm Interband Cascade "W" Laser", J. Electronic Materials, **27**, 77 (1998).

[24] S.R. White and L.J. Sham, "Electronic Properties of Flat-Band Semiconductor Heterostructures", Phys. Rev. Lett. **47**, 879 (1981).

[25] R. Q. Yang and J.M. Xu, "Analysis of transmission in polytype interband tunneling heterostructures", J. Appl. Phys. **72**, 4714 (1992).

[26] Z. Tian, L. Li, H. Ye, R.Q. Yang, T.D. Mishima, M.B. Santos, and M.B. Johnson, "InAs-based interband cascade lasers with emission wavelengths at 10.4 μm," *Electron. Lett*. **48**, 113–114 (2012).

[27] Y.-M. Mu, and Rui Q. Yang, "Theoretical investigation of mid-IR interband cascade lasers based on type-II quantum wells" J. App. Phys. **84**, 5357 (1998).
[28] R. Q. Yang, and Y. M. Mu, "Some Issues in Mid-IR Interband Cascade Lasers", Proc SPIE **3628,** pp. 104-112 (1999).
[29] H. Knotig, J. Nauschutz, N. Opacak, S. Hofling, J. Koeth, R. Weih, and B. Schwarz, "Mitigating valence intersubband absorption in interband cascade lasers", Laser & Photonics Reviews, 2200156 (2022).
[30] J. Nauschutz, H. Knotig, R. Weih, J. Scheuermann, J. Koeth, S. Hofling, and B. Schwarz, "Pushing the room temperature continuous-wave operation limit of GaSb-based interband cascade lasers beyond 6 μm", arXiv:2207.11113v1 [physics.optics], 2022.